


Kinetic characterization of multistep thermal oxidation of carbon/carbon composite in flowing air

Mechanical pencil leads as a model system

Kazuyuki Nishikawa¹ · Yumi Ueta¹ · Daichi Hara¹ · Shuto Yamada² · Nobuyoshi Koga¹ 

Received: 9 June 2016 / Accepted: 19 November 2016 / Published online: 3 December 2016
© Akadémiai Kiadó, Budapest, Hungary 2016

Abstract Thermal oxidation of carbon/carbon composites in an oxidizing atmosphere is a multistep process regulated by the intrinsic heterogeneity of the solid–gas reaction, the additional heterogeneity of the compositional and structural characteristics of the composite, and how these two properties change as the reaction progresses. By focusing on the overlapping features of the component reaction steps, the kinetic characterization of the multistep kinetic process was studied to reveal the correlation between the thermal oxidation behavior and the compositional and structural characteristics of carbon/carbon composites. Using commercially available mechanical pencil leads as a typical model system for a carbon/carbon composite, the thermal behaviors of two different leads manufactured by different companies were investigated comparatively via thermoanalytical techniques and morphological observations. On the basis of a reaction model considering the different reactivities of the main (graphite) and secondary (carbonized polymer) carbon components, the kinetic features of two partially overlapping reaction steps were revealed via a kinetic deconvolution analysis of the thermoanalytical data for the thermal oxidation process. The

kinetic results were correlated with the compositional and structural characteristics of carbon/carbon composites using morphological observations of the partially reacted samples. Herein, the practical usefulness of the kinetic analysis in characterizing carbon/carbon composites is discussed.

Keywords Carbon/carbon composite · Graphite · Thermal oxidation · Thermogravimetry · Reaction morphology · Kinetic deconvolution analysis

Introduction

The kinetics of the thermal oxidation of carbon/carbon composite materials in an oxidizing atmosphere have been extensively studied [1–17] because the thermal stability/resistibility of carbon materials is one of the most important factors in determining the potential applications of materials that effectively utilize their physical characteristics such as lightness, strength, and conductivities. Thermal oxidation of carbon is a complex solid–gas reaction because of the intrinsic heterogeneity of the reaction, as has been studied in detail for the oxidation reaction of graphite [18–28] and in many solid-state and solid–gas reactions [29–32]. In carbon/carbon composites, the situation is more complex because of the additional heterogeneity introduced by the compositional and structural factors of the composites [4, 6–8]. Therefore, kinetic characterization is forced to be phenomenological largely. Nevertheless, kinetic information is useful for evaluating the thermal stability of carbon/carbon composites in an oxidizing atmosphere and for refining carbon/carbon composite materials for wider applications under specific atmospheric conditions. In addition to contributing to

Electronic supplementary material The online version of this article (doi:10.1007/s10973-016-5993-6) contains supplementary material, which is available to authorized users.

✉ Nobuyoshi Koga
nkoga@hiroshima-u.ac.jp

¹ Department of Science Education, Graduate School of Education, Hiroshima University, 1-1-1 Kagamiyama, Higashi-Hiroshima 739-8524, Japan

² Department of Applied Chemistry, National Defense Academy of Japan, 1-10-20 Hashirimizu, Yokosuka 239-8686, Japan

materials science, kinetic understanding of the thermal oxidation of carbon/carbon composite materials can be applied to the combustion science of solid fuels involving biomass derivatives [33] and to the safety assessment of the storage of these fuels [34].

Generally, carbon/carbon composites comprise a main carbon component and a secondary carbon component, which binds the particles, tubes, or sheets of the main carbon component. The main and secondary carbon components have different reactivities because of their different crystallographic structures and morphologies. The junction characteristics of the main and secondary carbon components and pore structures in the composite are also responsible for regulating the reactivity to thermal oxidation [4, 6–8] because the pores are required to act as channels for diffusional intake of the reactant gas and diffusional removal of the product gas. A typical example of such a carbon/carbon composite is a mechanical pencil lead, which we use in our daily lives. In general, graphite and a polymer are used as the raw materials for preparing the leads. After mixing and kneading the main material (graphite) and the binder (polymer), rods are extruded. The molded rod is heated in an inert atmosphere so that it undergoes drying and calcination to increase its strength and hardness. During the calcination process, the polymer is carbonized, and consequently, a carbon/carbon composite is formed. The procedure is practically identical to that of many other carbon/carbon composites. In the manufacturing of pencil leads, the pores and interstices generated in the rod during the calcination process are filled with wax or oil by impregnation in the final step. Therefore, the compositional, structural, and physical properties of the as-produced carbon/carbon composite change with the properties of the main material, of the type of binder polymer, the mixed ratio of the main material to binder, and the calcination conditions of the molded intermediates. The kinetic characteristics of the thermal oxidation of a carbon/carbon composite appear to depend on all of the factors that determine its properties. In many kinetic studies on the thermal oxidation of carbon/carbon composites [1, 10, 13, 15, 16], the process has been recognized as a multistep reaction composed of two or three different kinetic steps, and different interpretations of the multistep kinetic behaviors have been proposed involving different rate-limiting steps of the chemical reaction and diffusion and different reaction behaviors of the carbon components. For example, Guo and Xiao [15] observed preferential oxidation of the matrix carbon component over fibers for the thermal oxidation of a carbon felt/carbon composite under isothermal conditions. Then, the two distinguishable reaction stages at a constant temperature were explained through kinetic analysis as the linear and nonlinear oxidation stages with different apparent

activation energies. In addition, the change in the rate-limiting step from the chemical reaction to gaseous diffusion as the reaction temperature increases was also discussed. A further extension of the kinetic interpretation of the thermal oxidation of carbon/carbon composites may be possible by considering the overlapping features of the multiple reaction steps involved. It is expected that a rigorous kinetic analysis of the multistep heterogeneous process that occurs during the thermal oxidation of carbon/carbon composites will provide us with relevant information to correlate the kinetic behavior with its compositional and structural characteristics, which will facilitate the improvement of the manufacturing process of carbon/carbon composites with desired properties and assessment of the practical usefulness of these materials.

The present study was carried out to reveal the empirical relationship between the multistep kinetic behavior of the thermal oxidation of a carbon/carbon composite in air and its compositional and structural properties. Mechanical pencil leads were selected as the model system because carbon/carbon composites with systematically changing compositional and structural characteristics are available as a series with different hardness or diameter size and different manufacturer suppliers. The aim of this study is to establish a test method for characterizing the compositional and structural properties of a carbon/carbon composite through kinetic analysis of its thermal oxidation process. Kinetic deconvolution analysis of the thermoanalytical data recently used to gain a detailed understanding of the various types of multistep solid-state and solid–gas reactions [35–42] was applied as the most suitable approach to describe the kinetic phenomena of the thermal oxidation process with the aid of the results of fundamental kinetic calculations and morphological observations of the samples during the reaction. This article reports a detailed comparison of the kinetic characteristics of the thermal oxidation processes of two different mechanical pencil leads manufactured by different companies as the first part of our study, which is expected to provide the necessary information to establish the methodology of kinetic analysis as a test method that is generally applicable to various carbon/carbon composites.

Experimental

Sample and characterization

Two commercially available mechanical pencil leads (0.5 mm diameter and hardness HB) manufactured by different companies in Japan were used as the samples and termed as A and B, respectively. The surface textures of the samples and those of the cleaved surfaces were observed

using a stereomicroscope (SZX7, Olympus) and scanning electron microscope (SEM; JSM-6510, JEOL). The powder X-ray diffraction (XRD) patterns of the samples crushed using an agate mortar and pestle were recorded using an instrument (RINT2200V, Rigaku Co.) with a monochrome Cu-K α (40 kV, 20 mA) in a range of $5^\circ \leq 2\theta \leq 60^\circ$ at a scan speed of 4° min^{-1} .

Tracking of thermal behavior

The pencil leads were cut into approximately 4 mm lengths for thermogravimetry–differential thermal analysis (TG–DTA; SSC/5200, SII). A single piece of sample (approximately 2.0 mg) was loaded onto a platinum pan (5 mm in diameter and 2.5 mm in height) and heated at a heating rate β of 5 K min^{-1} in flowing air ($300 \text{ cm}^3 \text{ min}^{-1}$). During the TG–DTA measurements, evolved gas analysis (EGA) for the outlet gas from the reaction chamber was simultaneously carried out using a CO $_2$ concentration meter (FX-720, IJIMA Co.). The gaseous products of the first mass-loss process were identified using pyrolysis–gas chromatography/mass spectrometry (Py–GC/MS), which consists of a double-shot pyrolyzer (PY-2020D, Frontier Lab.) coupled with a GC/MS (GC/MS-QP2010, Shimadzu). The samples (approximately 70 μg) were pyrolyzed in a stainless steel sample holder (50 mm^3) at 723 K for 0.1 s in flowing He ($50 \text{ cm}^3 \text{ min}^{-1}$), and the evolved gas was introduced into the GC column (UA5-30M-0.25F, 30 m in length and 0.25 mm inner diameter). The GC column was initially held at 343 K, then heated to 573 K at 20 K min^{-1} , and held at this temperature for 15 min. The outlet gas from the GC column was introduced into MS via a GC/MS interface heated at 573 K. Mass spectra were recorded by scanning in the range of 18–1100 m/z under electron impact ionization energy at 70 eV. Data analyses were performed with a Shimadzu GCMS solution (ver.4.20) to match the National Institute of Standards and Technology (NIST) Mass Spectra Library by comparison.

A single piece of the pencil lead (approximately 4 mm) was loaded onto a platinum pan (5 mm in diameter and 2.5 mm in height) and heated at a β of 5 K min^{-1} in air flow ($100 \text{ cm}^3 \text{ min}^{-1}$) to 1123 K in a heating stage equipped with an infrared image furnace (MS-TPS, Yonekura). The changes in the morphology of the samples during heating in the heating stage were observed using an optical microscope (BH-2, Olympus) and recorded as a movie together with time and temperature data.

The samples heated in the aforementioned TG–DTA to different temperatures were immediately cooled to room temperature in the instrument, and the as-prepared partially oxidized samples were observed using the stereomicroscope and SEM. At the same time as the SEM observation, the atomic contents of the samples were determined by

energy-dispersive X-ray (EDX) spectroscopy using an instrument (X-act, Oxford) equipped with the aforementioned SEM instrument.

Kinetic measurements

To record the kinetic rate data of the thermal oxidation process of the samples (0.5 mm in diameter and 4 mm in length, approximately 2 mg), the mass-loss data during isothermal and linear nonisothermal heating were measured using TG–DTA (SSC/5200, SII) in the flow of air ($300 \text{ cm}^3 \text{ min}^{-1}$). The flow rate of air was determined within the range in which the experimentally resolved shape of the TG–DTA curves is not influenced by the change in the flow rate, in order to avoid any possible influence of the change in O $_2$ concentration in the reaction atmosphere during the thermal oxidation reaction on the kinetic rate behavior [43]. The isothermal mass-change measurements were taken at different temperatures ($825 \leq T \leq 880 \text{ K}$) after heating the sample to each constant temperature at a β of 10 K min^{-1} . In the linear nonisothermal measurements, the samples were heated from room temperature to 1123 K at different β ($0.5 \leq \beta \leq 10 \text{ K min}^{-1}$). The thermal oxidation process of the samples was also tracked by a sample controlled thermal analysis (SCTA) technique [44] using a suspension-type TG (TGA-50, Shimadzu) equipped with a homemade SCTA controller [45–48]. The samples weighed in a platinum pan (6 mm in diameter and 2.5 mm in height) were heated in flowing air ($80 \text{ cm}^3 \text{ min}^{-1}$) at a β of 5 K min^{-1} , while during the thermal oxidation process the sample temperature was controlled so as to maintain the mass-loss rate at a constant value C of $7.5 \mu\text{g min}^{-1}$. A pair of SCTA measurements using one piece and two pieces of the sample rods (0.5 mm in diameter and 4 mm in length, approximately 2 mg each rod piece) was performed for each sample.

Results and discussion

Sample characterization

Stereomicroscopic views of the pencil lead samples are shown in Figure S1 in Supplementary Material. Figures 1 and 2 show SEM images of samples A and B, respectively. Irrespective of the samples, regularly arranged valleculeae along the direction of length were found (Figs. S1, 1a, 2a). The vallecule width of A (Fig. 1a) is apparently smaller than that of B (Fig. 2a). In both the samples, the surfaces show appearances that are coated with wax (Figs. 1b, 2b). However, the coating was thicker for A (Fig. 1b) than B (Fig. 2b). The cleaved surfaces of the pencil leads

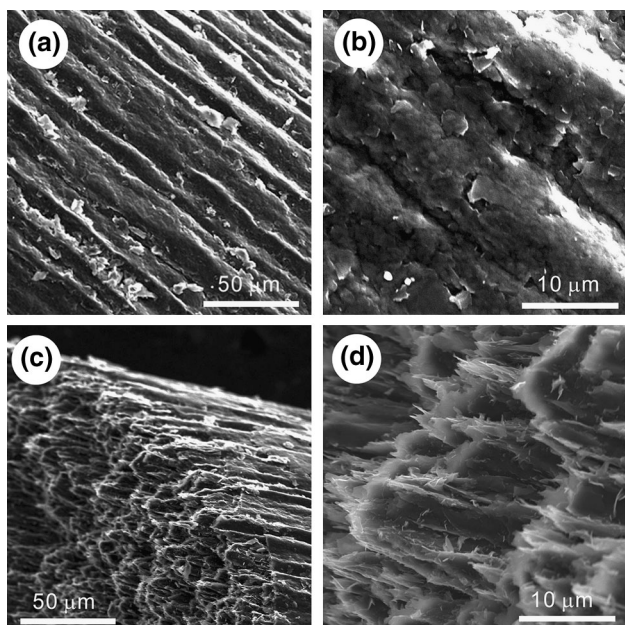


Fig. 1 SEM images of sample A: **a, b** surfaces, **c, d** cleaved surfaces

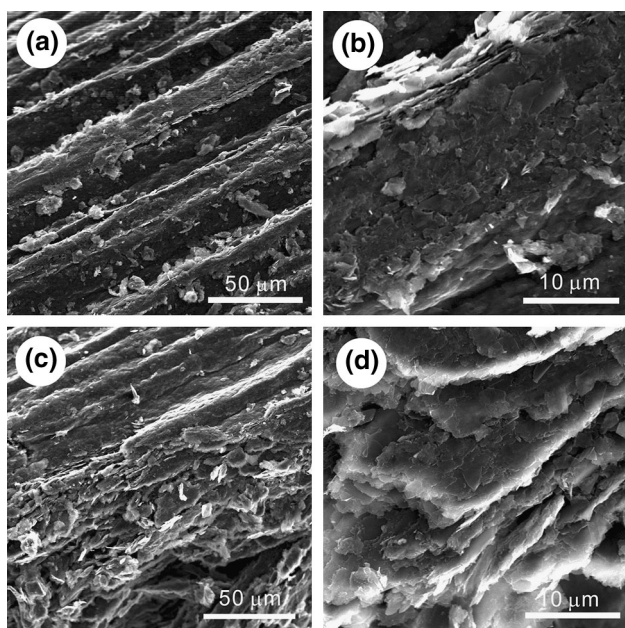


Fig. 2 SEM images of sample B: **a, b** surfaces, **c, d** cleaved surfaces

(Figs. 1c, 2c) also exhibit linearly arranged architectures along the direction of length. The internal architectures are constructed with aggregates of platelike graphite crystals (Figs. 1d, 2d). The aggregate in A (Fig. 1d) shows a brushed texture, whereas that of B (Fig. 2d) is brick-like. The XRD patterns of the samples are totally in accordance with that of graphite (hexagonal, S.G. = P63/mmc, $a = 2.47040$, $c = 6.72440$, JCPDS41-1487), as shown in Figure S2.

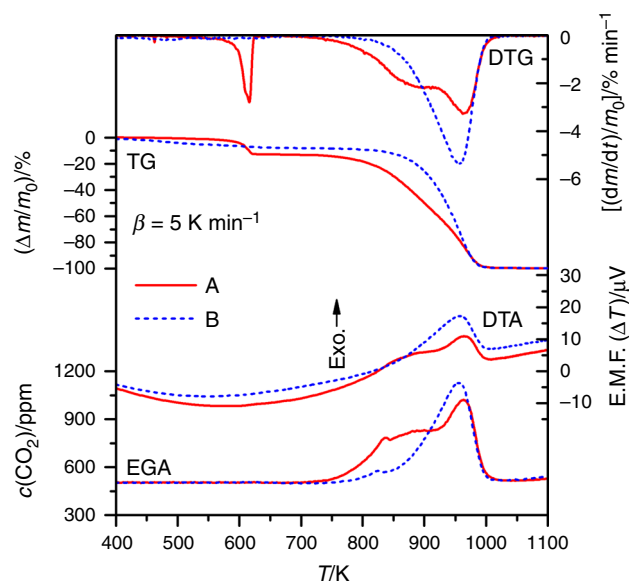


Fig. 3 TG–DTG–DTA–EGA (CO_2) curves for A ($m_0 = 2.17 \text{ mg}$) and B ($m_0 = 1.97 \text{ mg}$) samples in flowing air ($300 \text{ cm}^3 \text{ min}^{-1}$)

Thermal behaviors

Figure 3 shows the TG–DTG–DTA–EGA(CO_2) curves for samples A and B recorded in flowing air. Both of the samples exhibit mass loss without an accompanying production of CO_2 prior to the oxidation of the carbon materials. The initial mass loss of A occurs in a temperature region between 550 and 630 K with the mass-loss value of $13.0 \pm 0.5\%$, whereas that of B occurs in a wider temperature region between 430 and 700 K with the mass-loss value of $7.6 \pm 0.6\%$. These processes are likely attributed to the evaporation and degradation of wax. The subsequent mass loss due to the oxidation of carbon starts at approximately 720 K for A and 760 K for B with an exothermic effect and evolution of CO_2 . The shape of the TG, DTG, DTA, and EGA(CO_2) curves during the oxidation process was largely different for samples A and B. The thermoanalytical curves during the oxidation reaction for sample A clearly show the feature of overlapping two-step process, whereas those for sample B show relatively smooth thermoanalytical curves.

The pyrograms recorded for identifying the wax evaporated during the first mass-loss process of samples A and B are shown in Figure S3. The major peaks in the pyrogram of A are attributed to cyclic siloxane and 4-ethylacridine, which reveals the use of a silicon oil as an impregnation agent. From the peak area of the respective species, the major component of the organic antifriction is identified as 4-ethylacridine. Therefore, the sharp DTG peak observed at approximately 615 K in Fig. 3 is understood as the evaporation of 4-ethylacridine. The evaporation of cyclic polysiloxane, which has a lower boiling point than 4-ethylacridine, occurs at a lower

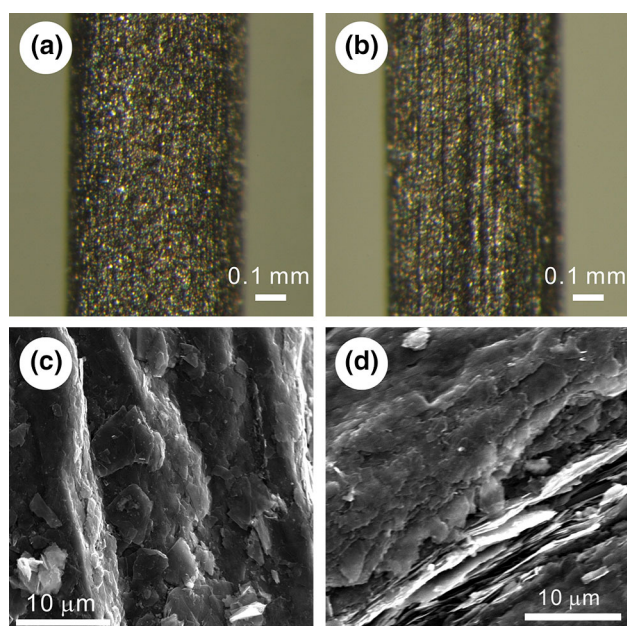


Fig. 4 Stereomicroscopic views (a, b) and SEM images (c, d) of the samples heated until the evaporation/degradation of wax was completed: a, c sample A heated to 651 K and b, d sample B heated to 676 K

temperature region, which is observed as a slight but detectable mass loss in the temperature range of 500–550 K. Sample B mainly comprises linear polyethylene with a large distribution of molecular mass. This may cause mass loss due to evaporation/degradation in a wide temperature region of 430–700 K.

Figure 4 shows the typical surface textures of samples A and B after the evaporation/degradation of wax. In both the samples, the molded rod shape is maintained during the thermally induced evaporation/degradation of wax (Fig. 4a, b). The SEM image of the surface texture of A (Fig. 4c) clearly shows the removal of the wax that coated the rod surfaces, revealing the graphite crystals that comprise the surface layer. For sample B, the change in the surface texture during the evaporation/degradation of wax was not as pronounced. This may be due to the smaller amount of wax involved in B, as is deduced from the smaller mass-loss value during the evaporation/degradation process observed in Fig. 3.

Figure S4 shows the EDX spectrum of the samples after the evaporation/degradation of wax was completed. In both the samples, impurities such as sodium and silicon were detected, as well as oxygen, which might be absorbed by carbon materials.

Oxidation kinetics

Figures 5 and 6 show the TG–DTG curves for the thermal oxidation of the samples recorded under linear

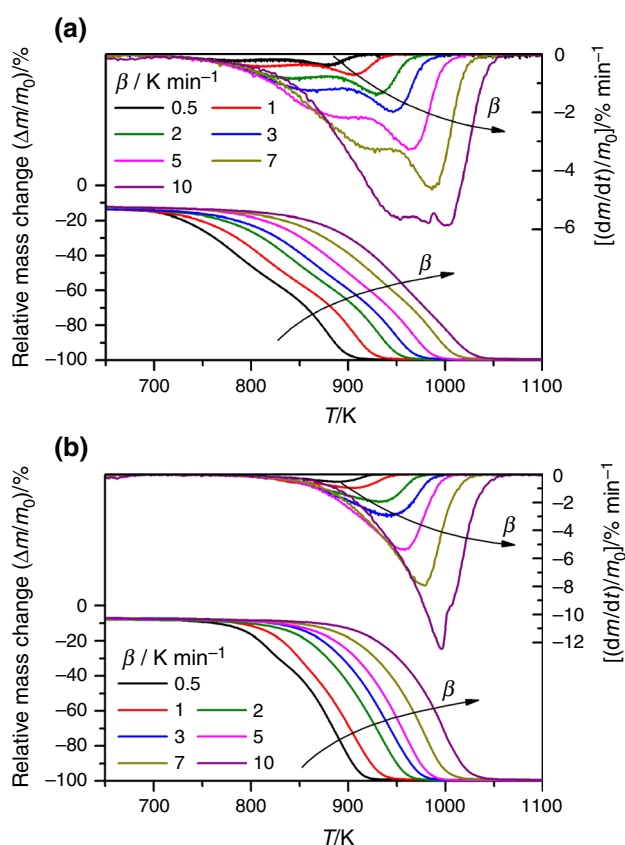


Fig. 5 Mass-change traces for the oxidation of pencil leads under linear nonisothermal conditions at different β in flowing air ($300 \text{ cm}^3 \text{ min}^{-1}$): a sample A and b sample B

nonisothermal conditions at different β and isothermal conditions at different T , respectively. The DTG curves of sample A indicate two distinguishable peaks during the reaction irrespective of those under linear nonisothermal (Fig. 5a) and isothermal conditions (Fig. 6a). The mass-loss process of sample B is relatively smooth at a higher β under linear nonisothermal conditions as characterized by the single DTG peak (Fig. 5b). However, a shoulder in the DTG peak appears in the early part of the mass-loss process at a β lower than 1 K min^{-1} . Under isothermal conditions, two DTG peak maxima are observed (Fig. 6b) as in sample A. The possible feature of the partially overlapping two-step process is more clearly seen from the results of the SCTA measurements because of its higher potential of experimental resolution for partially overlapping multistep processes in comparison with conventional thermal analysis [49–51]. Figure 7 shows the results of the SCTA measurements. During the thermal oxidation, the mass-loss rate was successfully controlled at a constant value (Fig. 7a, b). The temperature profiles of SCTA for the thermal oxidation process indicate two distinguishable regions of temperature change irrespective of the samples (Fig. 7c), initial reaction temperature drop, and subsequent

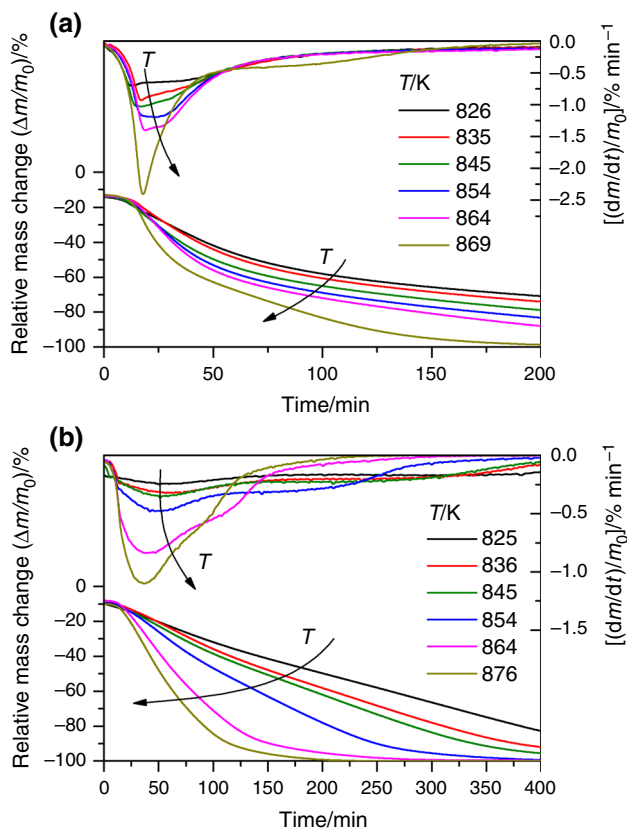


Fig. 6 Mass-change traces for the oxidation of pencil leads under isothermal conditions at different T in flowing air ($300 \text{ cm}^3 \text{ min}^{-1}$): **a** sample A and **b** sample B

gradual increase region from beginning of the reaction as the first temperature region and the nearly constant temperature and subsequent rapid increase region to the end of reaction as the second temperature region, which is evidence of the partially overlapping two-step process.

As the first kinetic approach to the oxidation reactions, kinetic analysis was performed based on the simplified kinetic equation that assumes a single-step reaction [24, 52].

$$\frac{d\alpha}{dt} = AS_0 \exp\left(-\frac{E_a}{RT}\right) f(\alpha) p(\text{O}_2)^X, \quad (1)$$

where α is the fractional reaction calculated by setting the total mass-loss value during the thermal oxidation reaction to be unity. S_0 , $p(\text{O}_2)$, and X are the initial surface area of the sample, partial pressure of oxygen in the reaction atmosphere, and reaction order with respect to oxygen concentration, respectively. A and E_a are the Arrhenius pre-exponential factor and the apparent activation energy, respectively. When S_0 and $p(\text{O}_2)$ were controlled to be respective constant values, the S_0 and $p(\text{O}_2)^X$ terms can be accommodated in A . The function $f(\alpha)$ denotes the kinetic model function that describes the variation of reaction rate

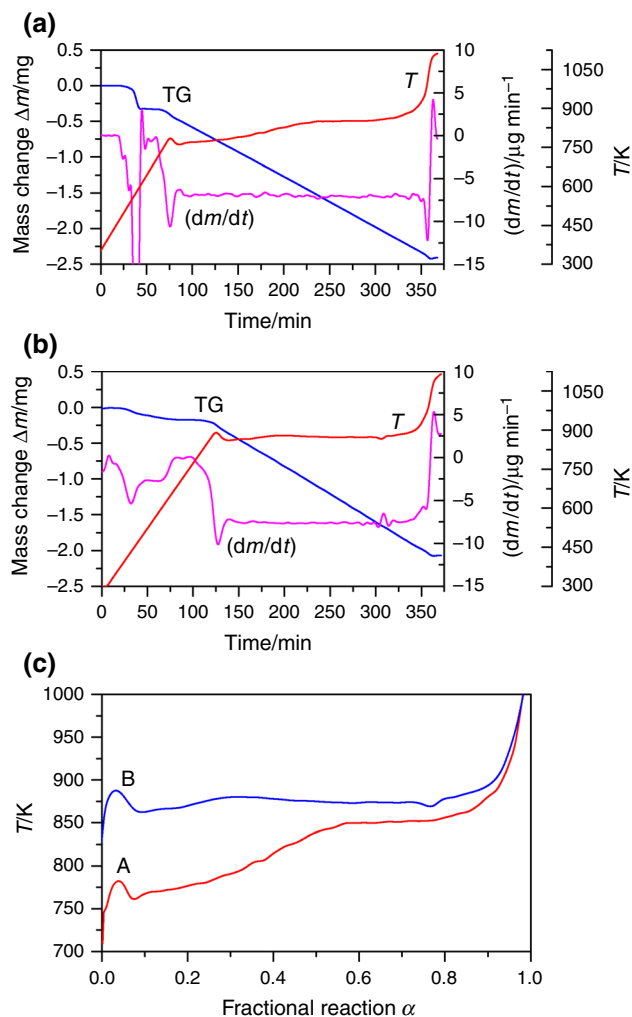


Fig. 7 Results of the SCTA measurements for the thermal oxidation process of the samples: **a** typical SCTA records for sample A ($m_0 = 2.460 \text{ mg}$, $C = 7.5 \text{ } \mu\text{g min}^{-1}$), **b** typical SCTA records for sample B ($m_0 = 2.024 \text{ mg}$, $C = 7.5 \text{ } \mu\text{g min}^{-1}$) and **c** temperature profile of the SCTA measurements of samples A and B during the course of the thermal oxidation reaction ($C = 7.5 \text{ } \mu\text{g min}^{-1}$)

as the reaction advances at a constant temperature and, thus, the physico-geometrical reaction mechanism. The functions for the solid-state reactions and that applicable to the oxidation reactions of solid fuels are found elsewhere [53]. Taking logarithms of both sides of Eq. 1,

$$\ln\left(\frac{d\alpha}{dt}\right) = \ln[Af(\alpha)] - \frac{E_a}{RT}. \quad (2)$$

Equation 2 denotes that the data points at a fixed α selected from the series of linear nonisothermal and isothermal kinetic rate data represent the linear relationship between $\ln(d\alpha/dt)$ and the reciprocal T . From the slope of the linear plots at fixed α , the E_a value is calculated, which is known as the Friedman plot [54] and is applicable to the kinetic rate data under any temperature profile [55–57].

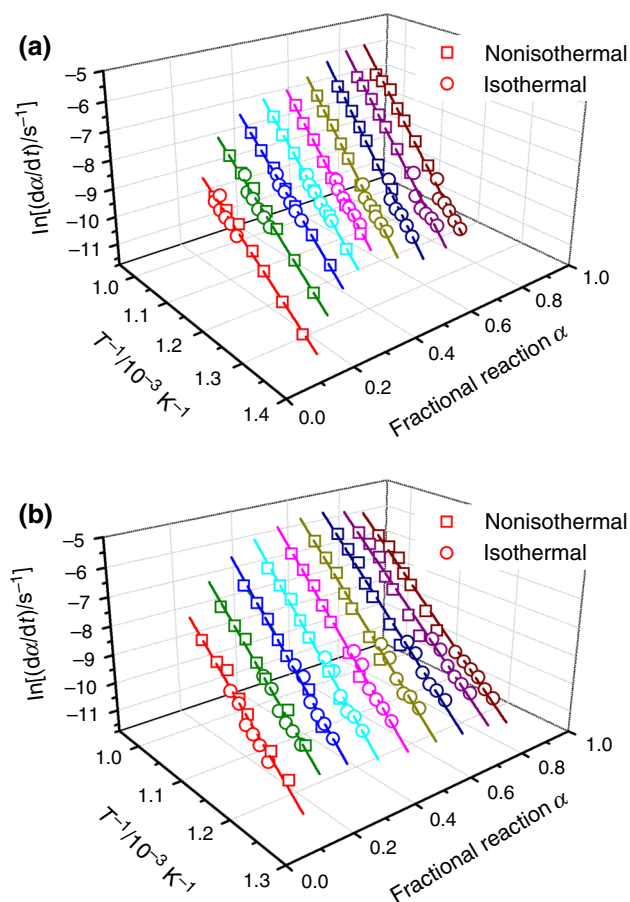


Fig. 8 Friedman plots for the oxidation of **a** sample A and **b** sample B

Figure 8 shows the Friedman plots for the oxidation reactions of samples A and B at different α from 0.1 to 0.9 in steps of 0.1 using the kinetic rate data recorded under linear nonisothermal and isothermal conditions. It must be noted that the Friedman plots indicate an acceptable linear relationship irrespective of α in both of the samples. This indicates that the oxidation reaction under linear nonisothermal and isothermal conditions can be treated by a unified formal kinetic feature in each sample. On the other hand, the slope of the Friedman plots changed gradually as the reaction advances. This behavior is not in accordance with that necessary for considering the reaction under investigation is fulfilled with the assumption of a single-step process [52]. Figure 9 shows the E_a values at different α , determined using the isoconversional kinetic relationship. The change in the slope of the Friedman plots can clearly be seen from the variation of E_a values (Fig. 9a). The E_a value for the oxidation of sample A increases initially from approximately $100\text{--}180\text{ kJ mol}^{-1}$ until α reaches approximately 0.65 and subsequently indicates a constant value with an average E_a value of $182.0 \pm 3.1\text{ kJ mol}^{-1}$ ($0.7 \leq \alpha \leq 0.9$). For the oxidation reaction of sample B, the E_a value initially increases from

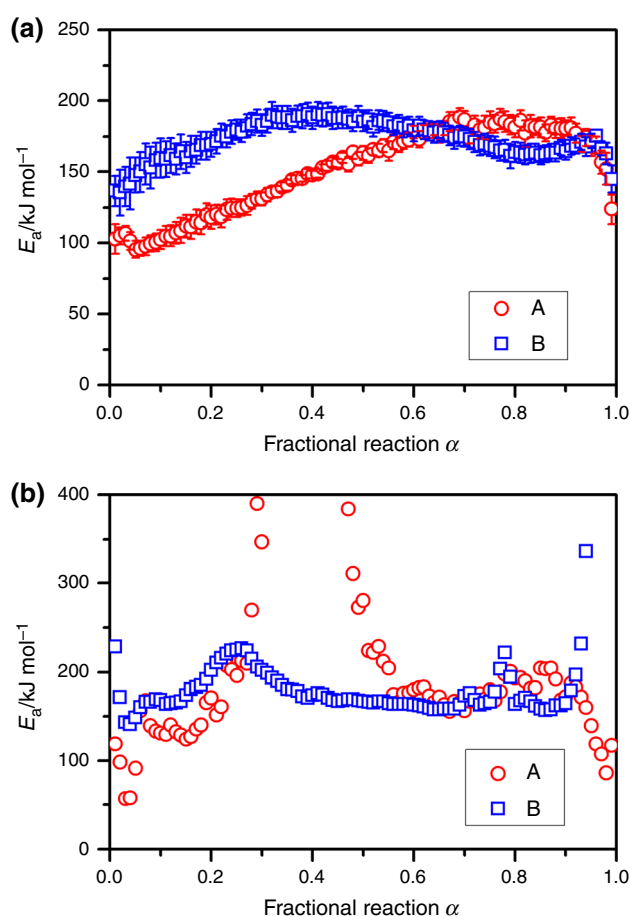


Fig. 9 Apparent E_a values at different α determined from: **a** the Friedman plots using the kinetic rate data under isothermal and linear isothermal conditions and **b** from Eq. 3 using the kinetic rate data under SCTA conditions

approximately $135\text{--}180\text{ kJ mol}^{-1}$ until α reaches approximately 0.35. The subsequent step can be expressed by a nearly constant E_a value with an average of $176.1 \pm 9.9\text{ kJ mol}^{-1}$ ($0.4 \leq \alpha \leq 0.9$). The trend of the variation of the E_a value as the reaction advances indicates that the overall oxidation reaction is composed of at least two partially overlapping reaction steps in both of the samples. In addition, it is expected that the contributions of the respective reaction step to the overall oxidation reaction are different between samples A and B, because the α range of the initial increase in the E_a value is largely different.

The overlapping feature of the two reaction steps can be more clearly seen from the variation of E_a evaluated from a pair of SCTA curves recorded for one piece and two pieces of pencil lead using a simplified isoconversional relationship between the two different sets of kinetic rate data (Fig. 9b) [58–60]:

$$E_{a,\alpha} = \frac{RT_1T_2}{T_1 - T_2} \ln \frac{(d\alpha/dt)_1}{(d\alpha/dt)_2} \quad (3)$$

The E_a values in Fig. 9b indicate characteristic α ranges with approximately constant values in the initial and final parts of the reaction that correspond to the nonoverlapping regions of the first and second reaction steps, respectively. On the other hand, in the α range between these constant E_a regions, an apparent jump in the E_a values is observed as a result of the overlapping of the two reaction steps. The differences in the E_a values between the first and second reaction steps reflect the different reactivities of the main and secondary carbon components in the carbon/carbon composite. At the same time, the differences in the E_a values in each initial and final constant E_a region between the samples are expected to reflect the different reactivities of each main and secondary carbon component between the samples. In addition, the E_a jump region and its range width are also different between the samples, $0.15 \leq \alpha \leq 0.55$ and $0.15 \leq \alpha \leq 0.35$ for A and B samples, respectively, from which the different composition of carbon/carbon composite and the different overlapping features of the thermal oxidation of the main and secondary carbon components are deduced.

From the above kinetic observations, it is apparent that a further detailed kinetic approach to the oxidation reaction requires the separation of the component reaction steps. When the mutual interactions of the component reaction steps are negligible, the overall rate behavior of the oxidation reaction is expressed by the cumulative kinetic equation of the two reaction steps [35–42].

$$\frac{d\alpha}{dt} = \sum_{i=1}^2 c_i A_i \exp\left(-\frac{E_{a,i}}{RT}\right) f_i(\alpha_i) \quad \text{with} \quad \sum_{i=1}^2 c_i = 1 \quad \text{and} \quad \sum_{i=1}^2 c_i \alpha_i = \alpha, \quad (4)$$

where c is the contribution of each reaction step to the overall reaction. The subscript i of each kinetic parameter specifies the reaction step, $i = 1$ or 2 . As the kinetic model function $f_i(\alpha_i)$, an empirical kinetic model function with three kinetic exponents was employed because of the high flexibility of the function to accommodate different types of physico-geometrical reaction mechanism and cases deviating from the idealized kinetic model [61–63].

$$f(\alpha) = \alpha^m (1 - \alpha)^n [-\ln(1 - \alpha)]^p \quad (5)$$

The function is known as Šesták–Berggren model [SB(m , n , p)] [61]. Therefore, kinetic analysis based on Eq. 4 requires the simultaneous determination of 12 kinetic parameters in total. Such kinetic deconvolution analysis is highly mathematical, and thus, the reliable determination of the initial values for the subsequent parameter optimization is the necessary condition to maintain the

significance of those parameters as the kinetic parameters. In this study, it was attempted to separate the overall kinetic rate data into two reaction steps using a mathematical method of peak deconvolution based on a statistical function [38, 64, 65]. Then, the separated kinetic rate data of each reaction step were analyzed kinetically using the formal kinetic equation for the single-step reaction, Eq. 1, to determine the initial kinetic parameters in Eq. 4 for the subsequent optimization. Details of the determination procedure of the initial kinetic parameters are described in Section S3.1 in Supplementary Material.

The initial values of the kinetic parameters in Eq. 4 were selected with reference to the kinetic parameters of each reaction step determined by formal kinetic analysis for the mathematically deconvoluted mass-loss curves, as listed in Table S1 in Supplementary Material. The c_i and $E_{a,i}$ values were substituted with the values listed in Table S1. The initial kinetic exponents in SB(m , n , p) of each reaction step were set as SB(0, 1, 0), which corresponds to the first-order kinetic equation, as was used in the kinetic fitting of the experimental master plots of the mathematically deconvoluted reaction steps (see Supplementary Material). After those values were placed in Eq. 4, the order of the initial A values of each reaction step was determined by comparing graphically the experimental kinetic rate data and that calculated using Eq. 4. Then, all of the kinetic parameters in Eq. 4 were optimized simultaneously using the nonlinear least squares method to minimize the squared sum of the difference between the experimental $(d\alpha/dt)_{\text{exp}}$ and calculated $(d\alpha/dt)_{\text{cal}}$ at different times.

$$F = \sum_{j=1}^M \left[\left(\frac{d\alpha}{dt} \right)_{\text{exp},j} - \left(\frac{d\alpha}{dt} \right)_{\text{cal},j} \right]^2 \quad (6)$$

Typical results of the kinetic deconvolution analysis are shown graphically in Fig. 10. The kinetic parameters of each reaction step optimized for the kinetic rate data recorded at different β were nearly identical. The results support the assumption of the overlapping of the kinetically independent processes, at least, in an empirical meaning. Table 1 lists the average kinetic parameters for each reaction step at different β . The contribution c_i of each reaction step i to the overall oxidation reaction is largely different between samples A and B, where a larger contribution of the first reaction step is observed for A. Although both of the first and second reaction steps of A are characterized by $E_{a,i}$ values smaller than those of B, both samples A and B indicate a larger $E_{a,i}$ value for the second reaction step than for the first reaction step. This trend well describes the temperature region of the respective reaction steps, which is higher for the second reaction steps. The A_i values of each reaction step vary with the change in the $E_{a,i}$ values, suggesting the possible behavior

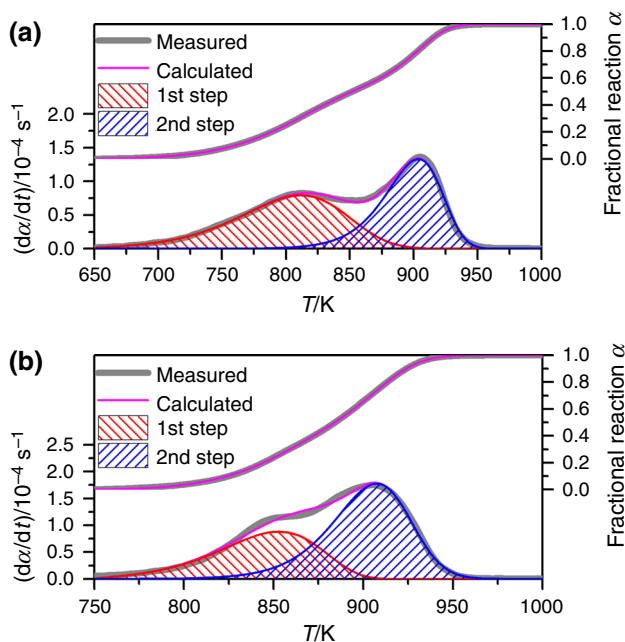


Fig. 10 Typical results of kinetic deconvolution for the oxidation reaction under a linear nonisothermal condition ($\beta = 1 \text{ K min}^{-1}$): **a** sample A and **b** sample B

of the kinetic compensation effect, which is an empirical linear relationship observed between E_a and $\ln A$ [66, 67]. Although it is a somewhat qualitative comparison because of the different kinetic model functions used for the evaluation of the Arrhenius parameters, the Arrhenius plots drawn using the optimized Arrhenius parameters of the first and second reaction steps of each sample and also those of the different samples in each reaction step were compared (see Figures S11 and S12 in Supplementary Material). The Arrhenius plots indicated a larger rate constant k for the first reaction step in the actual reaction temperature range, irrespective of the samples. When samples A and B were compared, the Arrhenius plots for sample A suggested a

larger k value in both the reaction steps. These observations are also in good agreement with the experimentally resolved shape and position of the mass-change traces of those two samples.

The rate behavior of the first and second reaction steps at a constant temperature is reproduced from the results of the kinetic deconvolution analysis shown in Table 1 according to [56, 57, 68, 69]:

$$\frac{d\alpha_i}{d\theta_i} = \frac{d\alpha_i}{dt} \exp\left(\frac{E_{a,i}}{RT}\right) = A_i f_i(\alpha_i) \quad \text{with} \quad (7)$$

$$\theta_i = \int_0^t \exp\left(-\frac{E_{a,i}}{RT}\right) dt$$

where θ is the Ozawa's generalized time [68, 69], which denotes the hypothetical reaction time at infinite temperature. As A_i is the constant for the single-step reaction, the $f_i(\alpha_i)$ versus α_i plot drawn using $\text{SB}(m_i, n_i, p_i)$ determined by kinetic deconvolution analysis can be recognized as the experimental master plot, which illustrates the change in the rate behavior as the reaction advances at infinite temperature [39, 42]. The experimental master plots are shown in Fig. 11, which clearly indicates the differences in the rate behaviors between the first and second reaction steps and also between samples A (Fig. 11a) and B (Fig. 11b). In the first reaction step, the experimental master plots for A indicate the linear deceleration as the reaction advances, which is perfectly fitted using a nucleation-and-growth-type model $\text{JMA}(m)$; $f(\alpha) = m(1 - \alpha)[- \ln(1 - \alpha)]^{1-1/m}$ [70–73], with $m = 1.00$, which corresponds exactly to a first-order reaction. On the other hand, the experimental master plot for the first step reaction of B indicates initial acceleration and subsequent deceleration with the maximum rate midway through the reaction and is empirically expressed by $\text{JMA}(1.32)$. The second reaction steps in A and B indicate a similar trend in the experimental master plot with the maximum midway through the reaction, which are fitted with $\text{JMA}(1.89)$ and $\text{JMA}(1.54)$,

Table 1 Average kinetic parameters of each reaction step for the thermal oxidation of samples A and B in flowing air, optimized through kinetic deconvolution analysis

Heating condition	Sample	i	c_i	$E_{a,i}/\text{kJ mol}^{-1}$	A_i/s^{-1}	$\text{SB}(m, n, p)$			R^2
						m_i	n_i	p_i	
Linear nonisothermal	A	1	0.56 ± 0.04	127.1 ± 1.7	$(5.0 \pm 0.2) \times 10^4$	-0.07 ± 0.13	1.02 ± 0.23	0.06 ± 0.11	0.999 ± 0.001
		2	0.44 ± 0.04	161.0 ± 1.5	$(1.9 \pm 0.8) \times 10^6$	0.20 ± 0.05	1.06 ± 0.09	0.35 ± 0.07	
	B	1	0.36 ± 0.02	134.4 ± 0.9	$(9.8 \pm 0.3) \times 10^4$	0.17 ± 0.06	1.03 ± 0.28	0.11 ± 0.02	0.999 ± 0.002
		2	0.64 ± 0.02	198.3 ± 1.0	$(1.9 \pm 0.1) \times 10^8$	0.18 ± 0.03	1.00 ± 0.10	0.21 ± 0.04	
Isothermal	A	1	0.57 ± 0.04	129.2 ± 2.6	$(4.8 \pm 0.9) \times 10^4$	-0.04 ± 0.04	0.96 ± 0.10	0.08 ± 0.03	0.992 ± 0.004
		2	0.43 ± 0.04	164.4 ± 2.5	$(1.8 \pm 0.2) \times 10^6$	0.17 ± 0.04	0.94 ± 0.19	0.27 ± 0.12	
	B	1	0.39 ± 0.02	135.6 ± 0.8	$(9.7 \pm 0.1) \times 10^4$	0.23 ± 0.01	1.07 ± 0.03	0.13 ± 0.01	0.988 ± 0.002
		2	0.61 ± 0.02	191.7 ± 0.9	$(1.7 \pm 0.1) \times 10^8$	0.29 ± 0.01	1.19 ± 0.05	0.39 ± 0.03	

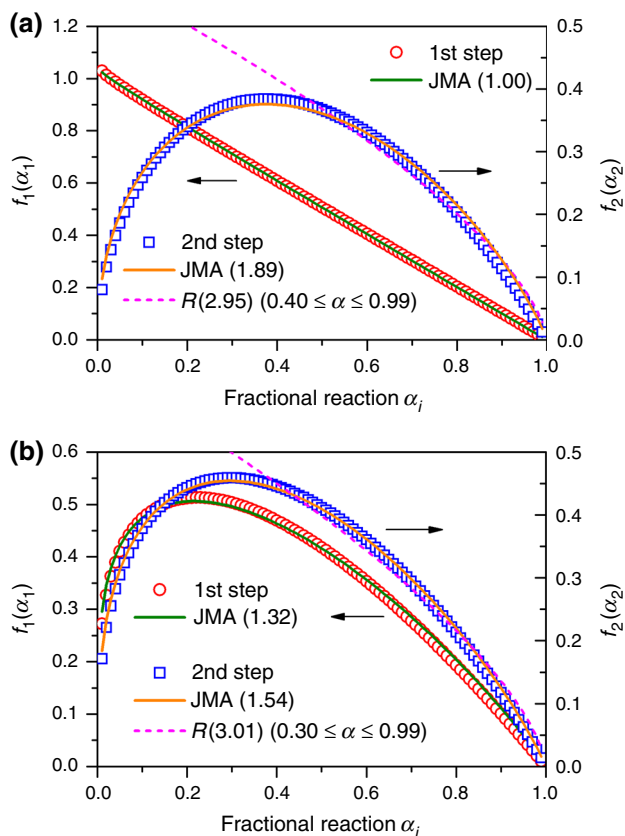


Fig. 11 Experimental master plots of $f_i(\alpha_i)$ versus α_i drawn using the SB(m_i, n_i, p_i) determined by the kinetic deconvolution analysis: **a** sample A and **b** sample B

respectively. In addition, the deceleration parts of the second reaction step of both the samples are similarly fitted using the phase boundary-controlled reaction model $R(n)$ [74]; $f(\alpha) = n(1 - \alpha)^{1-1/n}$ with approximately $n = 3$. All of these experimental master plots of the first and second reaction steps of A and B cannot be described by a simple contracting geometry-type kinetic model for the solid–gas reactions involving the ideal two-dimensional shrinkage of columnar rod and the platelike graphite crystals. The rate behavior of the oxidation of graphite with the maximum rate midway through the reaction has been reported by Badenhorst and Focke [25] for synthetic Kish graphite. This behavior has been explained by the complex reaction geometry caused by the development of randomly distributed holes in the rectangular graphite flakes [22]. In the present system of a carbon/carbon composite, the idea can be further extended to the destruction of the framework of the rod composition and the structure of the carbon/carbon composite as the reaction advances.

As the isoconversional relationship was confirmed with acceptable linearity of the Friedman plots at different α applied to the overall reaction under linear nonisothermal and isothermal conditions (Fig. 8), the rate behaviors under

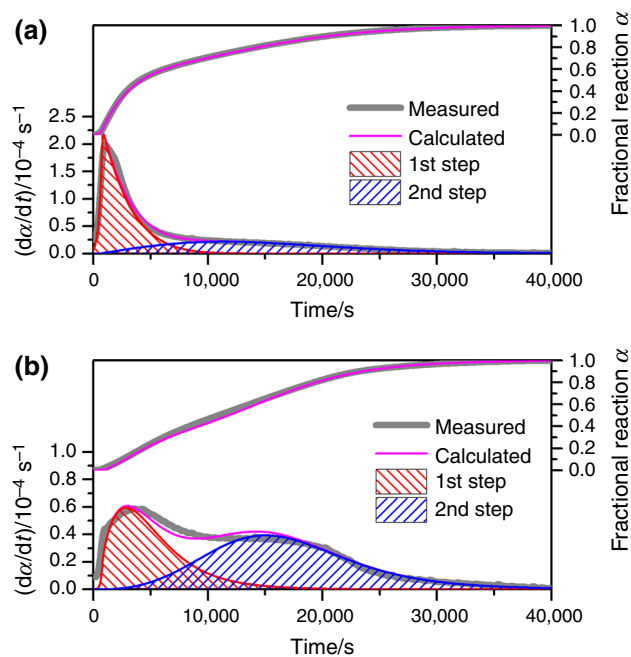


Fig. 12 Typical results of the kinetic deconvolution for the oxidation reaction under isothermal conditions ($T = 845$ K): **a** sample A and **b** sample B

those temperature conditions were expected to be nearly identical. Therefore, the kinetic rate data under isothermal conditions were also subjected to kinetic deconvolution analysis using the optimized kinetic parameters for the reactions under linear nonisothermal conditions as the initial parameters. Figure 12 shows the typical results of the kinetic deconvolution analysis for the reactions of samples A (Fig. 12a) and B (Fig. 12b) under isothermal conditions. The optimized kinetic parameters are also listed in Table 1. Irrespective of the samples, the experimental kinetic rate data under isothermal conditions were satisfactorily fitted with optimized kinetic parameters, which are practically identical to those optimized for reactions under linear nonisothermal conditions. This observation means that neither the contribution nor kinetic behavior of each reaction step changes over the examined temperature region.

Microscopic appearance during the oxidation reaction

Figure 13 shows selected video frames of the movies recorded during the heating of samples A (Fig. 13a) and B (Fig. 13b) at 5 K min^{-1} in flowing air ($100 \text{ cm}^3 \text{ min}^{-1}$). Irrespective of which sample was used, no significant changes in the molded rod shape and its diameter size were observed between the optical microscopic views of just before the start of the oxidation reaction [Fig. 13a(1), b(1)] and at the maximum reaction rate of the first reaction step

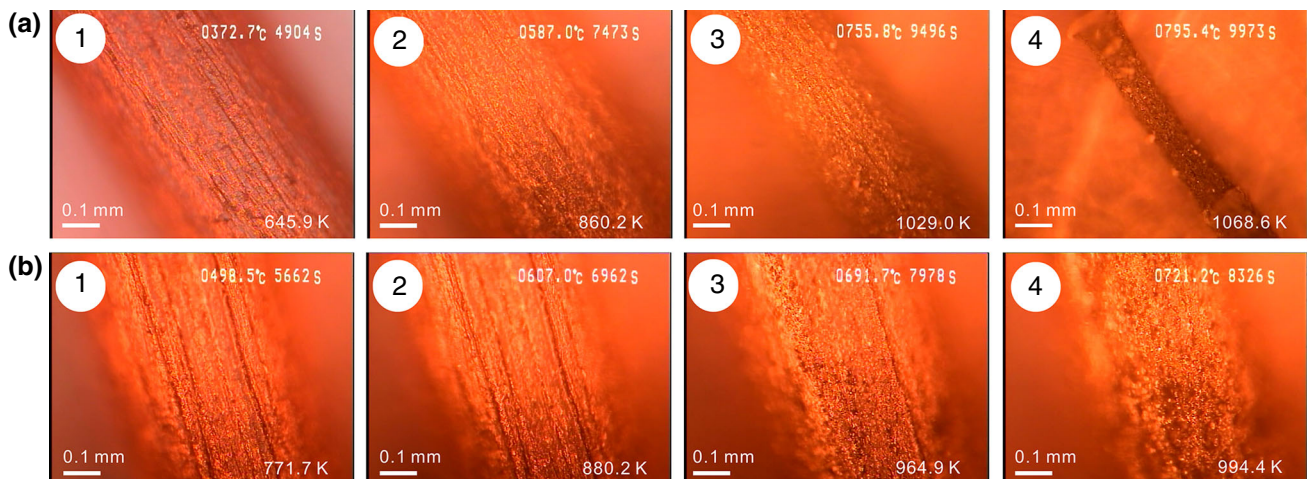


Fig. 13 Microscopic views of each sample during heating at 5 K min^{-1} in flowing air ($100 \text{ cm}^3 \text{ min}^{-1}$): **a** sample A and **b** sample B

[Fig. 13a(2), b(2)], although many light spots caused by the surface oxidation were observed during the first reaction step of the thermal oxidation. During the temperature region of the second reaction step, those samples exhibited apparently different morphological changes. During the second reaction step of sample A, the diameter size of the rod continuously decreased as the reaction advances [Fig. 13a(3), a(4)] and finally disappeared leaving small traces of impurity ash. In the case of sample B, the diameter size of the rod is maintained during the major part of the second reaction step [Fig. 13b(3)]. Then, the rod becomes a mere facade with the formation of many holes and interstices [Fig. 13b(4)]. In the final part of the second reaction step, the rod shrinks suddenly and disappears.

Figures 14 and 15 show the SEM images of samples A and B, heated at 5 K min^{-1} in flowing air ($300 \text{ cm}^3 \text{ min}^{-1}$) to different temperatures in the range of oxidation reactions of each sample, respectively. The surface textures of A heated to approximately the maximum reaction rate of the first reaction step (Fig. 14a) exhibit each platelike crystal of graphite more clearly than that observed before the initiation of the oxidation reaction (Fig. 4a). In the temperature region where the shrinkage of rod tends to occur, the individual graphite crystals are more clearly separated on the surfaces of the rod and many voids are formed between those graphite crystals (Fig. 14b). At this reaction stage, the rod surfaces are coated with a surface shell (Fig. 14c). In the rod interior (Fig. 14d), the brushed texture observed for the original sample A (Fig. 1d) disappeared and the stacking structure of the platelike graphite crystals is clearly observed. The morphological characteristics of sample A at the second reaction step indicates that shrinkage of the rod occurs by simultaneous oxidation reactions on the surface of the rod and the internal graphite constructions by maintaining the surface graphite shell.

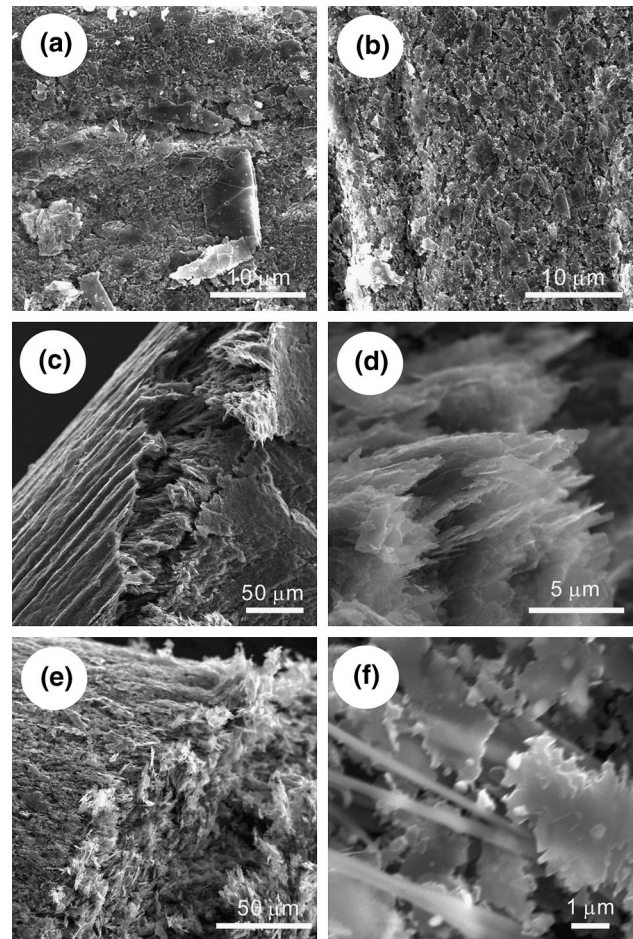


Fig. 14 SEM images of sample A heated to different temperatures in flowing air ($300 \text{ cm}^3 \text{ min}^{-1}$) at 5 K min^{-1} : **a** 850 K ($\alpha = 0.16$), **b–d** 923 K ($\alpha = 0.52$), and **e, f** 981 K ($\alpha = 0.86$)

During the final part of the second reaction step, the difference in the structure of the graphite crystals on the surface and interior of the rod is not distinguishable

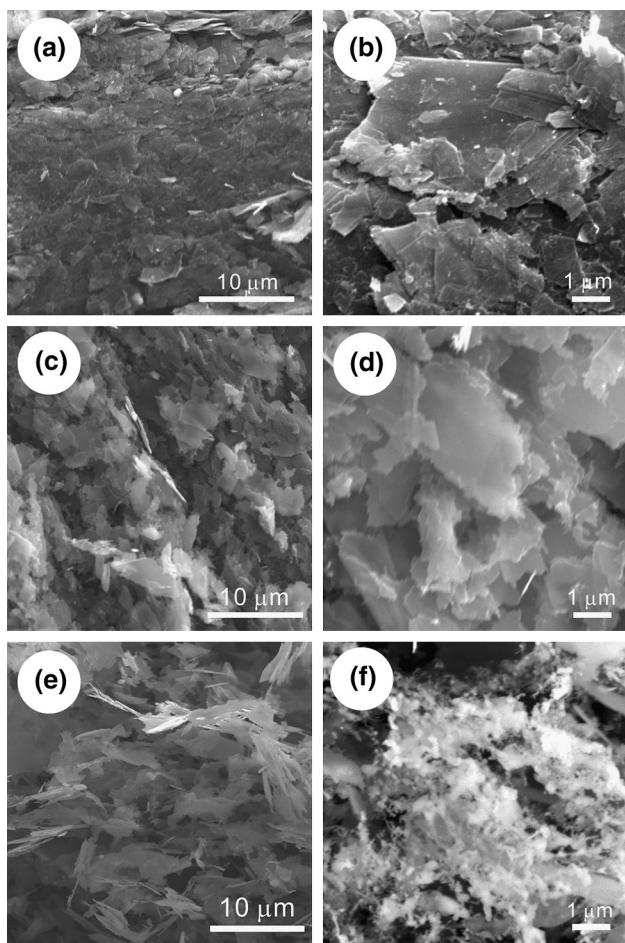


Fig. 15 SEM images of sample B heated to different temperatures in flowing air ($300 \text{ cm}^3 \text{ min}^{-1}$) at 5 K min^{-1} : **a, b** 877 K ($\alpha = 0.04$), **c, d** 943 K ($\alpha = 0.29$), and **e, f** 1000 K ($\alpha = 0.85$)

(Fig. 14e). At this stage, many needlelike outshoots irradiating from the voids between the graphite crystals are observed (Fig. 14f), presumably impurity ash.

At the temperature corresponding to approximately the maximum reaction rate of the first reaction step of sample B (Fig. 15a), the surface texture is smoother than that of sample A at the corresponding reaction stage (Fig. 14a). However, formation of voids between graphite crystals is observed in larger magnification views (Fig. 15b). In the temperature region of the second reaction step, the surface of the rod is largely modified with the formation of large voids and holes (Fig. 15c). From the change in shape of the platelike graphite crystals from those at the first reaction step (Fig. 15b) to the second reaction stage (Fig. 15d), the edge surfaces of the platelike crystals are recognized as the reaction sites. Therefore, the oxidation reaction of each graphite crystal occurs in the geometrical scheme of two-dimensional shrinkage, as has been reported for the reaction of dispersed graphite crystals [25]. The formation of large voids and holes in the rod

surface at the second reaction step may promote the oxidation reaction in the interior of the rod, rendering the rod a mere facade. At the final stage of the second reaction step of sample B, the thin graphite crystals are dispersed with large voids (Fig. 15e), irrespective of the surface or interior of the rod. This leads to the sudden constraint of the rod at the end of the reaction. At this stage, many filaments dispersed throughout the entirety of the sample are observed, which is thought to be the ash of impurities (Fig. 15f).

Figure S5 shows the EDX spectrum of the samples at the final stage of the graphite oxidation, which contains impurities that became obvious from SEM observations (Figs. 14f, 15f). In comparison with the sample before the graphite oxidation (Figure S4), the content ratio of the impurity atoms with reference to carbon apparently increased. This appears to result from the increase in the relative impurity content by the oxidation of carbon. A larger content ratio of impurities was identified for sample A. The major impurity atom is silicon in both the samples. For sample A, sodium and oxygen are also detected, indicating that the sodium silicate compound is the residue of the oxidation. On the other hand, the content of aluminum is larger than sodium in sample B. The difference in the morphology of the impurities between samples A and B observed in Figs. 14f and 15f, respectively, is probably caused by the difference in the relative content ratio and the chemical contents of impurities.

Practical usefulness of the kinetic deconvolution analysis

From the preparation procedure of the graphite rods for mechanical pencils and SEM observations, it can be deduced that the graphite rods are constructed from the graphite crystals originally mixed for the preparation and the interstitial carbon component produced from polymer mixed as a binder during the calcination of the molded mixture, as well as smaller amounts of clay. Therefore, the mechanical pencil leads have the typical compositional and structural features of a carbon/carbon composite material. As the second reaction step of the thermal oxidation is characterized by the oxidation of the originally mixed graphite crystals as observed using SEM (Figs. 14b–d, 15c, d), the first reaction step appears to be attributed to the oxidation reaction of the carbon component, which was produced in the manufacturing process by the carbonization of the polymer and filled up the interstices of the larger graphite crystals. Therefore, a two-step reaction feature as revealed by the kinetic study of the oxidation reaction can be interpreted as results from the different reactivities and kinetic behaviors of the carbon components in the carbon/carbon composite. The contribution of each reaction step to the overall oxidation reaction reflects the content of each carbon

component in the composite. Comparing samples A and B, the larger contribution of the first reaction step observed for sample A indicates that the content of the carbon component originating from calcination of the polymer binder was larger for A. From the viewpoint of characterization of the carbon/carbon composite, the kinetic deconvolution analysis examined in this study for the thermally induced oxidation of the mechanical pencil lead in air is useful for the compositional analysis of the carbon/carbon composite.

In addition to the information concerning the composition, kinetic deconvolution analysis provides kinetic information of each reaction step of the thermal oxidation of the composite, which can be used for characterizing the reactivity of each carbon component. The thermal oxidation of each carbon component is a heterogeneous process that is controlled by the crystallinity and crystal morphology, including size and shape of the crystal. Impurities may also influence the oxidation kinetics as catalysts [9, 11, 17]. In addition, the propagation of the active surface of carbon for the oxidation is enhanced as the reaction advances by the development of pin holes, cracks, etc. [14, 22, 25]. It is thus expected that the properties and conditions of each carbon component in the composite can be relatively deduced from the different overall kinetic behavior of the reaction of each carbon component revealed through the kinetic deconvolution analysis. In addition to the comparison of the E_a and A values between the respective reaction steps and among the different samples, differences in the rate behavior at a constant temperature as deduced from the experimental master plot of $f_i(\alpha_i)$ versus α_i appear to be useful for characterizing empirically the nature of each carbon component. The rate behavior of the second reaction step can be correlated with the crystallographic and morphological characteristics of the graphite mixed originally. By comparing the apparent kinetic behaviors of the thermal oxidation of the raw and the manufactured graphite in the molded carbon/carbon composite, it is expected that a change in the reactivity by the manufacturing can be deduced. As far as the present samples A and B are concerned, the apparent kinetic behavior of the second reaction step is illustrated by a similar experimental master plot that exhibits a maximum rate midway through the reaction, although larger $E_{a,2}$ and A_2 values were obtained for B in comparison with A. In contrast, the rate behavior of the first oxidation process is largely different between the samples. The linear deceleration of the reaction rate as the reaction advances observed for A indicates the adherence to the first-order rate law and the simple consumption of the reactant, while the rate behavior of the first reaction step of B resembles that of the second reaction step, exhibiting the maximum reaction rate midway through the reaction. The carbon component that reacts in the first reaction step is generated by the carbonization of the

polymer during the calcination of mold injected graphite rod. Therefore, the thermal oxidation behavior of the first reaction step varies with the mixed polymer, calcination conditions, crystallographic, and morphological properties of the as-produced graphite or amorphous carbon particles, and the structural characteristics of the carbon/carbon composite. Furthermore, the overlapping feature of the thermal oxidation of the two carbon components appears to vary depending on the nature of each carbon component, the conjunction between the components, the construction of the composite, and its changes as the reaction advances. Therefore, the overlapping features of the multistep oxidation process revealed in this study by applying kinetic deconvolution analysis can be a relative measure for characterizing the carbon/carbon composite.

Although the analysis method is largely empirical and phenomenological due to the complex heterogeneity of the reaction, the multistep kinetic behavior of the thermal oxidation of carbon/carbon composites revealed using kinetic deconvolution analysis will probably be useful for characterizing the composites as overall phenomena, which reflect their compositional, crystallographic, and structural characteristics. Kinetic information can be used as a reference for determining the appropriate mixing ratio of the mother mixture and processing conditions for preparing the composite and for the product management. The practical usability is demonstrated in separated articles by applying the kinetic deconvolution analysis to the thermal oxidation process of mechanical pencil leads manufactured by different companies and also to a series of mechanical pencil leads with different hardness.

Conclusions

Everyday mechanical pencil leads manufactured by the calcination of a graphite and polymer binder mixture have the typical structural features of carbon/carbon composites with two carbon components: one is the originally mixed graphite, and the other is formed during the calcination process by the carbonization of the polymer binder. The thermal behavior of the two different pencil leads manufactured by different companies was comparatively investigated in this study. On heating the mechanical pencil lead in flowing air, the evaporation/degradation of wax or oil is detected as the first mass-loss process. The organic antifriction used and the total mass loss during evaporation/degradation are different among the pencil leads manufactured by different companies. The mass-loss value during the evaporation/degradation of the organic antifriction can be the empirical measurement of pores and its structure in the carbon/carbon composite for comparing the series of the carbon/carbon composite when the same

wax or oil has been used. Subsequently, the thermally induced oxidation of the carbon components occurs in two partially overlapping reaction steps irrespective of the sample. The specific features of the two overlapping reaction steps were confirmed by applying isoconversional kinetic analysis to the overall oxidation process with an assumption of a single-step reaction. The results clearly indicated the change in the apparent E_a value as the reaction advances and the constant E_a region in the latter half of the overall reaction. The shift point of the two characteristic E_a regions was different between the pencil leads. Based on the results of the isoconversional kinetic analysis, the overall reaction was separated into two reaction steps using kinetic deconvolution analysis, which assumes independent kinetic processes, after a preliminary kinetic calculation for the empirically deconvoluted kinetic curves using a mathematical deconvolution method. From the results of the kinetic deconvolution analysis, the contributions of each reaction step to the overall reaction were determined. In addition, the kinetic behavior of each reaction step was characterized separately through determining the Arrhenius parameters and empirical kinetic model functions. The Arrhenius parameters reasonably described the relative thermal stability between the component reaction steps and between the samples. The empirical kinetic model function was used for drawing the experimental master plot of each reaction step, which simulates the change in the rate behavior at a constant temperature. Different rate behaviors of the first reaction step were estimated for the different samples, while rate behaviors that resembled the reported kinetic features of the thermal oxidation of graphite particles were observed for the second reaction step, irrespective of the sample. From the morphological study, it was confirmed that the first reaction step of the thermal oxidation proceeds by maintaining the original diameter and shape of the rod in both the samples. Simultaneously, the outline of the graphite particles became sharper during the first reaction step. Although the changing behavior of the rod size and shape during the second reaction step was different between the samples, two-dimensional shrinkage and thinning of each platelike graphite particle were evident. These observations illustrate that the thermal oxidation of the carbon component produced during the calcination of the graphite–thermoplastic mixed mold and of the graphite particles originally mixed in the mold occur in the first and second reaction steps, respectively. Therefore, the kinetic results of the thermal oxidation process of the carbon/carbon composite obtained using kinetic deconvolution analysis provide information concerning the composition of the carbon/carbon composite and the kinetic features of each reaction step, which reflects the crystallographic and structural characteristics of each carbon component. On the

basis of the present study, kinetic analysis of the thermal oxidation processes is proposed to be a technique that can be used to characterize carbon/carbon composites, which is useful for determining the preparation conditions of the composite and for product control.

Electronic supplementary material

Sample characterization (optical microscopic views, powder XRD patterns); thermal behavior (pyrograms for the evolved gases, EDX spectra); thermal oxidation kinetics using a mathematical deconvolution technique; Interpretation of apparent Arrhenius parameters.

Acknowledgements The present work was supported by JSPS KAKENHI Grant Nos. 25242015 and 16K00966.

References

1. Dačić B, Marinković S. Kinetics of air oxidation of unidirectional carbon fibres/CVD carbon composites. *Carbon*. 1987;25(3):409–15.
2. McKee DW. Oxidation behavior and protection of carbon/carbon composites. *Carbon*. 1987;25(4):551–7.
3. Crocker P, McEnaney B. Oxidation and fracture of a woven 2D carbon-carbon composite. *Carbon*. 1991;29(7):881–5.
4. Shemet VZ, Pomytkin AP, Neshpor VS. High-temperature oxidation behaviour of carbon materials in air. *Carbon*. 1993;31(1):1–6.
5. Han JC, He XD, Du SY. Oxidation and ablation of 3D carbon-carbon composite at up to 3000 °C. *Carbon*. 1995;33(4):473–8.
6. Bacos MP, Dorvaux JM, Lavigne O, Renollet Y. C/C composite oxidation model: I. Morphological experimental investigations. *Carbon*. 2000;38(1):77–92.
7. Bacos MP, Cochon JL, Dorvaux JM, Lavigne O. C/C composite oxidation model: II. Oxidation experimental investigations. *Carbon*. 2000;38(1):93–103.
8. Bacos MP, Dorvaux JM, Lavigne O, Talandier J. C/C composite oxidation model: III. Physical basis, limitations and applications. *Carbon*. 2000;38(1):105–17.
9. Park S-J, Seo M-K. The effects of MoSi₂ on the oxidation behavior of carbon/carbon composites. *Carbon*. 2001;39(8):1229–35.
10. Luo R, Cheng J, Wang T. Oxidation behavior and protection of carbon/carbon composites prepared using rapid directional diffused CVI techniques. *Carbon*. 2002;40(11):1965–72.
11. Wu X, Radovic LR. Catalytic oxidation of carbon/carbon composite materials in the presence of potassium and calcium acetates. *Carbon*. 2005;43(2):333–44.
12. Gao P, Guo W, Xiao H, Guo J. Model-free kinetics applied to the oxidation properties and mechanism of three-dimension carbon/carbon composite. *Mater Sci Eng, A*. 2006;432(1–2):226–30.
13. Guo W, Xiao H, Yasuda E, Cheng Y. Oxidation kinetics and mechanisms of a 2D-C/C composite. *Carbon*. 2006;44(15):3269–76.
14. Jacobson NS, Curry DM. Oxidation microstructure studies of reinforced carbon/carbon. *Carbon*. 2006;44(7):1142–50.
15. Guo W, Xiao H. Mechanisms and modeling of oxidation of carbon felt/carbon composites. *Carbon*. 2007;45(5):1058–65.

16. Hou X-M, Chou K-C. A simple model for the oxidation of carbon-containing composites. *Corros Sci.* 2010;52(3):1093–7.
17. Bevilacqua M, Babutskyi A, Chrysanthou A. A review of the catalytic oxidation of carbon–carbon composite aircraft brakes. *Carbon.* 2015;95:861–9.
18. Makino A, Araki N, Mihara Y. Combustion of artificial graphite in stagnation flow: estimation of global kinetic parameters from experimental results. *Combust Flame.* 1994;96(3):261–74.
19. Loren Fuller E, Okoh JM. Kinetics and mechanisms of the reaction of air with nuclear grade graphites: IG-110. *J Nucl Mater.* 1997;240(3):241–50.
20. Bews IM, Hayhurst AN, Richardson SM, Taylor SG. The order, Arrhenius parameters, and mechanism of the reaction between gaseous oxygen and solid carbon. *Combust Flame.* 2001;124(1–2):231–45.
21. Zaghbi K, Song X, Kinoshita K. Thermal analysis of the oxidation of natural graphite: isothermal kinetic studies. *Thermochim Acta.* 2001;371(1–2):57–64.
22. Breval E, Klimkiewicz M, Agrawal DK, Rusinko F. Pinhole formation and weight loss during oxidation of industrial graphite and carbon. *Carbon.* 2002;40(7):1017–27.
23. Hurt RH, Haynes BS. On the origin of power-law kinetics in carbon oxidation. *Proc Combust Inst.* 2005;30(2):2161–8.
24. Yang H-C, Eun H-C, Lee D-G, Jung C-H, Lee K-W. Analysis of combustion kinetics of powdered nuclear graphite by using a non-isothermal thermogravimetric method. *J Nucl Sci Technol.* 2006;43(11):1436–9.
25. Badenhorst H, Focke WW. Geometric effects control isothermal oxidation of graphite flakes. *J Therm Anal Calorim.* 2012;108(3):1141–50.
26. Badenhorst H, Focke W. Comparative analysis of graphite oxidation behaviour based on microstructure. *J Nucl Mater.* 2013;442(1–3):75–82.
27. Badenhorst H, Rand B, Focke W. A generalized solid state kinetic expression for reaction interface-controlled reactivity. *Thermochim Acta.* 2013;562:1–10.
28. Gaddam CK, Vander Wal RL, Chen X, Yezerets A, Kamasamudram K. Reconciliation of carbon oxidation rates and activation energies based on changing nanostructure. *Carbon.* 2016;98:545–56.
29. Galwey AK, Brown ME. *Thermal decomposition of ionic solids.* Amsterdam: Elsevier; 1999.
30. Galwey AK. Structure and order in thermal dehydrations of crystalline solids. *Thermochim Acta.* 2000;355(1–2):181–238.
31. Koga N, Tanaka H. A physico-geometric approach to the kinetics of solid-state reactions as exemplified by the thermal dehydration and decomposition of inorganic solids. *Thermochim Acta.* 2002;388(1–2):41–61.
32. Pijolat M, Favregeon L, Soustelle M. From the drawbacks of the Arrhenius- $f(\alpha)$ rate equation towards a more general formalism and new models for the kinetic analysis of solid–gas reactions. *Thermochim Acta.* 2011;525(1–2):93–102.
33. Branca C, Di Blasi C. Combustion kinetics of secondary biomass chars in the kinetic regime. *Energy Fuels.* 2010;24(10):5741–50.
34. Qiu Y, Collin F, Hurt RH, Külaots I. Thermochemistry and kinetics of graphite oxide exothermic decomposition for safety in large-scale storage and processing. *Carbon.* 2016;96:20–8.
35. Sánchez-Jiménez PE, Perejón A, Criado JM, Diáñez MJ, Pérez-Maqueda LA. Kinetic model for thermal dehydrochlorination of poly(vinyl chloride). *Polymer.* 2010;51(17):3998–4007.
36. Koga N, Suzuki Y, Tatsuoka T. Thermal dehydration of magnesium acetate tetrahydrate: formation and in situ crystallization of anhydrous glass. *J Phys Chem B.* 2012;116(49):14477–86.
37. Sánchez-Jiménez PE, Pérez-Maqueda LA, Perejón A, Criado JM. Nanoclay nucleation effect in the thermal stabilization of a polymer nanocomposite: a kinetic mechanism change. *J Phys Chem C.* 2012;116(21):11797–807.
38. Koga N, Goshi Y, Yamada S, Pérez-Maqueda LA. Kinetic approach to partially overlapped thermal decomposition processes. *J Therm Anal Calorim.* 2013;111(2):1463–74.
39. Koga N, Yamada S, Kimura T. Thermal decomposition of silver carbonate: phenomenology and physico-geometrical kinetics. *J Phys Chem C.* 2013;117(1):326–36.
40. Noda Y, Koga N. Phenomenological kinetics of the carbonation reaction of lithium hydroxide monohydrate: role of surface product layer and possible existence of a liquid phase. *J Phys Chem C.* 2014;118(10):5424–36.
41. Kitabayashi S, Koga N. Thermal decomposition of tin(II) hydroxide and subsequent oxidation in air: kinetic deconvolution of overlapping heterogeneous processes. *J Phys Chem C.* 2015;119(28):16188–99.
42. Nakano M, Fujiwara T, Koga N. Thermal decomposition of silver acetate: physico-geometrical kinetic features and formation of silver nanoparticles. *J Phys Chem C.* 2016;120(16):8841–54.
43. Vyazovkin S, Chrissafis K, Di Lorenzo ML, Koga N, Pijolat M, Roduit B, Sbirrazzuoli N, Suñol JJ. ICTAC Kinetics Committee recommendations for collecting experimental thermal analysis data for kinetic computations. *Thermochim Acta.* 2014;590:1–23.
44. Sørensen OT, Rouquerol J. *Sample controlled thermal analysis: origin goals, multiple forms, applications and future.* Dordrecht: Kluwer; 2003.
45. Alcalá MD, Criado JM, Gotor FJ, Ortega A, Pérez-Maqueda LA, Real C. Development of a new thermogravimetric system for performing constant rate thermal analysis (CRTA) under controlled atmosphere at pressures ranging from vacuum to 1 bar. *Thermochim Acta.* 1994;240:167–73.
46. Koga N, Criado JM. The influence of mass transfer phenomena on the kinetic analysis for the thermal decomposition of calcium carbonate by constant rate thermal analysis (CRTA) under vacuum. *Int J Chem Kinet.* 1998;30(10):737–44.
47. Diáñez MJ, Pérez Maqueda LA, Criado JM. Direct use of the mass output of a thermobalance for controlling the reaction rate of solid-state reactions. *Rev Sci Instrum.* 2004;75(8):2620–4.
48. Criado JM, Pérez-Maqueda LA, Diáñez MJ, Sánchez-Jiménez PE. Development of a universal constant rate thermal analysis system for being used with any thermoanalytical instrument. *J Therm Anal Calorim.* 2007;87(1):297–300.
49. Criado JM, Pérez-Maqueda LA. Sample controlled thermal analysis and kinetics. *J Therm Anal Calorim.* 2005;80(1):27–33.
50. Sánchez-Jiménez PE, Pérez-Maqueda LA, Crespo-Amoros JE, Lopez J, Perejón A, Criado JM. Quantitative characterization of multicomponent polymers by sample-controlled thermal analysis. *Anal Chem.* 2010;82(21):8875–80.
51. Pérez-Maqueda LA, Criado JM, Sánchez-Jiménez PE, Diáñez MJ. Applications of sample-controlled thermal analysis (SCTA) to kinetic analysis and synthesis of materials. *J Therm Anal Calorim.* 2015;120(1):45–51.
52. Koga N. Ozawa's kinetic method for analyzing thermoanalytical curves. *J Therm Anal Calorim.* 2013;113(3):1527–41.
53. Khawam A, Flanagan DR. Solid-state kinetic models: basics and mathematical fundamentals. *J Phys Chem B.* 2006;110(35):17315–28.
54. Friedman HL. Kinetics of thermal degradation of cha-forming plastics from thermogravimetry, application to a phenolic plastic. *J Polym Sci C.* 1964;6:183–95.
55. Ozawa T. Applicability of Friedman plot. *J Therm Anal.* 1986;31:547–51.

56. Koga N. Kinetic analysis of thermoanalytical data by extrapolating to infinite temperature. *Thermochim Acta*. 1995;258:145–59.
57. Gotor FJ, Criado JM, Málek J, Koga N. Kinetic analysis of solid-state reactions: the universality of master plots for analyzing isothermal and nonisothermal experiments. *J Phys Chem A*. 2000;104(46):10777–82.
58. Koga N, Yamada S. Influences of product gases on the kinetics of thermal decomposition of synthetic malachite evaluated by controlled rate evolved gas analysis coupled with thermogravimetry. *Int J Chem Kinet*. 2005;37(6):346–54.
59. Yamada S, Koga N. Kinetics of the thermal decomposition of sodium hydrogen carbonate evaluated by controlled rate evolved gas analysis coupled with thermogravimetry. *Thermochim Acta*. 2005;431(1–2):38–43.
60. Koga N, Goshi Y, Yoshikawa M, Tatsuoka T. Physico-geometrical kinetics of solid-state reactions in an undergraduate thermal analysis laboratory. *J Chem Educ*. 2014;91(2):239–45.
61. Šesták J, Berggren G. Study of the kinetics of the mechanism of solid-state reactions at increasing temperatures. *Thermochim Acta*. 1971;3:1–12.
62. Šesták J. Diagnostic limits of phenomenological kinetic models introducing the accommodation function. *J Therm Anal*. 1990;36(6):1997–2007.
63. Šesták J. Rationale and fallacy of thermoanalytical kinetic patterns. *J Therm Anal Calorim*. 2011;110(1):5–16.
64. Perejón A, Sánchez-Jiménez PE, Criado JM, Pérez-Maqueda LA. Kinetic analysis of complex solid-state reactions. A new deconvolution procedure. *J Phys Chem B*. 2011;115(8):1780–91.
65. Svoboda R, Málek J. Applicability of Fraser–Suzuki function in kinetic analysis of complex crystallization processes. *J Therm Anal Calorim*. 2013;111(2):1045–56.
66. Koga N. A review of the mutual dependence of Arrhenius parameters evaluated by the thermoanalytical study of solid-state reactions: the kinetic compensation effect. *Thermochim Acta*. 1994;244(1):1–20.
67. Galwey AK, Mortimer M. Compensation effects and compensation defects in kinetic and mechanistic interpretations of heterogeneous chemical reactions. *Int J Chem Kinet*. 2006;38(7):464–73.
68. Ozawa T. A new method of analyzing thermogravimetric data. *Bull Chem Soc Jpn*. 1965;38(11):1881–6.
69. Ozawa T. Non-isothermal kinetics and generalized time. *Thermochim Acta*. 1986;100(1):109–18.
70. Avrami M. Kinetics of phase change. I. General theory. *J Chem Phys*. 1939;7(12):1103–12.
71. Avrami M. Kinetics of phase change. II. Transformation-time relations for random distribution of nuclei. *J Chem Phys*. 1940;8(2):212–23.
72. Avrami M. Granulation, kinetics of phase change. III. Phase change, and microstructure. *J Chem Phys*. 1941;9(2):177–84.
73. Barmak K. A commentary on: “reaction kinetics in processes of nucleation and growth”. *Metall Mater Trans A*. 2010;41(11):2711–75.
74. Spencer WD, Topley B. Reaction velocity in the system $\text{Ag}_2\text{CO}_3 \leftrightarrow \text{Ag}_2\text{O} + \text{CO}_2$. *Trans Faraday Soc*. 1931;27:94–102.